Japanese Journal of Applied Physics

The Japan Society of Applied Physics

REGULAR PAPER • OPEN ACCESS

Precise determination of polarization fields in c-plane GaN/Al $_x$ Ga$_{1-x}$ N/GaN heterostructures with capacitance–voltage-measurements

To cite this article: Norman Susilo *et al* 2019 *Jpn. J. Appl. Phys.* **58** SCCB08

OPEN ACCESS

Japanese Journal of Applied Physics **58**, SCCB08 (2019) **REGULAR PAPER**

https://doi.org/10.7567/1347-4065/ab09dd

Precise determination of polarization fields in c-plane GaN/Al$_x$Ga$_{1-x}$N/GaN heterostructures with capacitance–voltage-measurements

Norman Susilo[1*], Marcel Schilling[1], Michael Narodovitch[2], Hsin-Hung Yao[3], Xiaohang Li[3], Bernd Witzigmann[4], Johannes Enslin[1], Martin Guttmann[1], Georgios G. Roumeliotis[1], Monir Rychetsky[1], Ingrid Koslow[1], Tim Wernicke[1], Tore Niermann[2], Michael Lehmann[2], and Michael Kneissl[1]

[1]*Institute of Solid State Physics, Technische Universität Berlin, Hardenbergstraße 36, Berlin, Germany*
[2]*Institute of Optics and Atomic Physics, Technische Universität Berlin, Hardenbergstraße 36, Berlin, Germany*
[3]*King Abdullah University of Science and Technology (KAUST), Advanced Semiconductor Laboratory, Thuwal, 23955, Saudi Arabia*
[4]*Universität Kassel, Computational Electronics and Photonics Group and CINSaT, Kassel, Germany*

[*]E-mail: norman.susilo@physik.tu-berlin.de

Received December 17, 2018; accepted February 7, 2019; published online April 23, 2019

Due to changes in the spontaneous and piezoelectric polarization, AlGaN/GaN heterostructures exhibit strong polarization fields at heterointerfaces. For quantum wells, the polarization fields lead to a strong band bending and a redshift of the emission wavelength, known as quantum-confined Stark effect. In this paper the polarization fields of thin AlGaN layers in a GaN matrix were determined by evaluating the changes in the depletion region width in comparison to a reference sample without heterostructure using capacitance–voltage-measurements. The polarization fields for Al$_{0.09}$Ga$_{0.91}$N (0.6 ± 0.7 MV cm^{-1}), Al$_{0.26}$Ga$_{0.74}$N (2.3 ± 0.6 MV cm^{-1}), Al$_{0.34}$Ga$_{0.66}$N (3.1 ± 0.6 MV cm^{-1}), Al$_{0.41}$Ga$_{0.59}$N (4.0 ± 0.7 MV cm^{-1}) and Al$_{0.47}$Ga$_{0.53}$N (5.0 ± 0.8 MV cm^{-1}) heterostructures were determined. The results of the field strength and field direction of all samples are in excellent agreement with values predicted by theory and a capacitance–voltage based Poisson-carrier transport simulation approach giving experimental evidence for a nonlinear increasing polarization field with Al-concentration.

1. Introduction

AlGaN/GaN heterostructures are commonly used for electronic and optoelectronic devices such as field-effect transistors for high power, high temperature and high voltage operation[1–4] and in LEDs and laser diodes[5–11] either as quantum well or as electron blocking layer. The low-symmetry of wurtzite crystals leads to a non-zero spontaneous polarization field in equilibrium causing polarization sheet charges at AlGaN/GaN interfaces due to the large difference in spontaneous polarization.[2,12] Furthermore, high macroscopic piezoelectric polarization fields are generated in pseudomorphically grown heterostructures due to lattice mismatch (i.e. strain) and large piezoelectric coefficients in AlGaN.[2,13–15] The resulting polarization field is in the order of MV cm^{-1}[16,17] and leads to a strong band bending.[18–20] In order to correctly describe and understand the carrier transport and recombination in GaN/AlGaN/GaN semiconductor devices, an accurate determination of the magnitude and direction of the polarization fields is of great importance. Unfortunately, very few publications concerning the quantitative measurement of the internal fields in GaN/AlGaN/GaN optical devices exist.

In this paper we precisely determine the polarization fields in GaN/AlGaN/GaN heterostructures based on capacitance–voltage-measurements (CVM). By evaluating the changes in the depletion region width of *pin* diodes caused by the polarization sheet charges at the interfaces, we are able to determine the polarization fields with high accuracy. To evaluate the polarization fields based on an analytical model,[21] it is necessary to compare the depletion region width of a reference sample without the heterostructure (i.e. homojunction) to a sample with a heterostructure. In addition, the polarization fields were extracted from the CVM with the help of self-consistent Poisson and drift-diffusion calculations using the internal polarization charges as a fitting parameter. Both methods are based on the change of the depletion region with changing polarization field. The error analysis shows that the accuracy of the results depends strongly on the thickness of the heterostructure and the error of the CVM. For an accurate determination of the capacitance and in order to minimize the error, transmission electron microscopy (TEM) measurements were performed and a more accurate equivalent circuit directly related to the sample structure has been developed, tested, and applied.

2. Experiment

The *pin* diode heterostructures were grown by metalorganic vapor phase epitaxy on (0001) c-plane sapphire substrates. Details of the sample structure are shown in Fig. 1. A GaN-based buffer layer was deposited, followed by a 1 μm thick n^+ GaN:Si current spreading layer with a nominal Si-doping level of 3×10^{18} cm^{-3}, a 100 nm thick GaN:Si doping gradient and a 400 nm thick low doped n^- GaN:Si layer with a nominal Si-concentration of 1×10^{17} cm^{-3}. The 25 nm thick intrinsic region consists of a 5 nm thick Al$_x$Ga$_{1-x}$N layer embedded in a GaN matrix. Finally the heterostructure was capped by a 150 nm thick p^+ GaN:Mg layer with a nominal Mg-concentration of 8×10^{18} cm^{-3} and a 10 nm thick p^{++} GaN:Mg contact layer. The heterostructures were processed into *pin* diodes by standard microfabrication techniques using Ti-based *n*-contacts and Ni/Au *p*-contacts. The CVM were performed on 100×100 μm^2 *p*-contacts, which define the capacitance area A.

A set of samples with different Al-compositions in the 5 nm thick Al$_x$Ga$_{1-x}$N layer were fabricated ($x = 0.09$, 0.26, 0.34, 0.41, 0.47). Additionally, a reference sample was grown without a heterostructure (i.e. $x = 0$) in the intrinsic

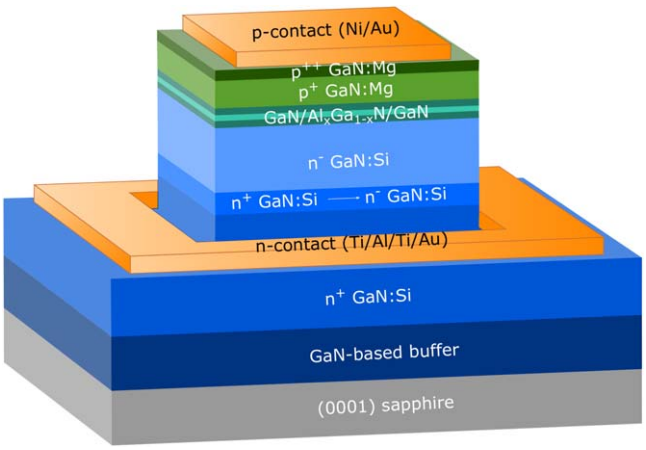

Fig. 1. (Color online) Sample structure of the GaN-based *pin* diode grown on (0001) sapphire.

region. The Al-content was determined by high resolution X-ray diffraction (HRXRD) $\omega - 2\theta$ measurements close to the (0002) GaN reflection on calibration samples. The capacitance values are determined from impedance-frequency measurements by a Keysight E4980A Precision LCR Meter assuming next to the capacitance parallel resistances as well as series resistances (see Sect. 3). To determine the thickness of the $Al_xGa_{1-x}N$ layer, TEM was performed in an aberration corrected TEM operated at 300 kV (FEI-Titan).

To determine the internal polarization fields of these *pin* diodes, CVM were performed. As recently published[21,22] the internal polarization field E_{Pol} can be written as

$$E_{\mathrm{Pol}} = \frac{1}{d_{\mathrm{DHS}}}\left\{V_{\mathrm{ref}} - V - \frac{2k_BT}{q} - \left(\frac{\partial}{\partial V}\frac{1}{C^2}\right)^{-1} \cdot \left(\frac{d_u^2}{\epsilon_0^2\epsilon_r^2A^2}\cdot\frac{(N_D - N_i)(N_A + N_i)}{N_AN_D} - \frac{1}{C^2}\right)\right\}, \quad (1)$$

where

$$V_{\mathrm{ref}} = V + \frac{2k_B\widetilde{T}}{q} + \left(\frac{\partial}{\partial V}\frac{1}{\widetilde{C}^2}\right)^{-1} \cdot \left(\frac{\widetilde{d_u}^2}{\epsilon_0^2\widetilde{\epsilon_r}^2\widetilde{A}^2}\cdot\frac{(\widetilde{N_D} - \widetilde{N_i})(\widetilde{N_A} + \widetilde{N_i})}{\widetilde{N_A}\widetilde{N_D}} - \frac{1}{\widetilde{C}^2}\right), \quad (2)$$

d_u describes the thickness of the intrinsic region, N_A and N_D are the acceptor and donor concentrations of the *p*- and *n*-doped regions respectively, N_i is the *n*-type background doping concentration in the intrinsic region, ϵ_0 is the vacuum permittivity, ϵ_r is the relative permittivity, q is the elementary charge, V_{ref} is the reference potential, d_{DHS} is the thickness of the layer of interest in the double heterostructure, T is the temperature, k_B is the Boltzmann constant and V is an additional external bias voltage. Values with a tilde symbol correspond to values of the reference structure. The reference potential V_{ref} can be calculated using the reference sample. Since no heterojunction is included in the reference sample, neither a change in the spontaneous polarization nor a change in the piezoelectric polarization occurs, and therefore no total polarization at all. Consequently, the reference potential can be extracted from the CVM without a superposition with a polarization field. It is important to note that the reference potential V_{ref} is in principle equal to the build-in potential V_{bi} of the pin-diode. However, parasitic electric fields (generated by Fermi level pinning or Schottky contacts) can lead to a deviation of the reference potential V_{ref} from the build-in potential V_{bi}. Since $N_A \gg N_D$, the *n*-doping concentration can be determined from the voltage derivative of the capacitance–voltage measurement

$$N_D = -\left[\frac{q\epsilon_o\epsilon_rA^2}{2}\frac{\partial}{\partial V}\left(\frac{1}{C^2}\right) + \frac{1}{N_A}\right]^{-1}. \quad (3)$$

Alternatively the polarization field can be determined by matching the experimental *CV*-curves with a coupled Poisson-carrier transport simulation of the *pin* diode as recently published.[21,22] The polarization charges and therefore the polarization field are used as parameters for matching the experimental *CV*-curves. By fitting also the *CV* curves of the reference sample the doping profile was extracted and employed for the heterostructure samples. Note that Eq. (1) assumes a constant doping profile, while the CVM-based Poisson-carrier transport simulation approach also includes non-constant doping profiles extracted from the CVM.

Parameter	Relative error	Parameter	Relative error
d_{DHS}	5%	$\widetilde{\epsilon_r}$, ϵ_r	10%
$\partial/\partial V\ \widetilde{C}^{-2}$, $\partial/\partial V\ C^{-2}$	2%	$\widetilde{d_u}$, d_u	5%
$\widetilde{C}$, C	3%	$\widetilde{T}$, T	10%
$\widetilde{A}$, A	10%	$\widetilde{N_A}$, N_A	100%
$\widetilde{N_D}$, N_D	50%	$\widetilde{N_i}$, N_i	100%

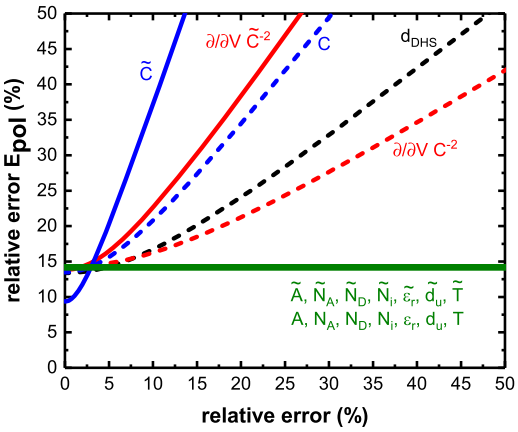

Fig. 2. (Color online) Relative error of the polarization field evaluated by Gaussian error propagation as a function of the relative error of every parameter in Eq. (1). Solid lines correspond to parameters of the reference sample and dashed lines to parameters of the heterostructure sample.

3. Accuracy of the polarization field evaluation

In this section, the measurement error is discussed. In general, errors can be caused by deviations of the sample structure from the nominal structure used for the evaluation, e.g. the background doping in the intrinsic region, layer thicknesses and doping deviations during growth and process deviations between the *pin* diodes. Equation (1) depends on 18 parameters containing uncertainties. Figure 2 shows the estimated relative errors of each parameter. To determine the influence of each parameter we varied each error from 0% up to +50% while all the other values and parameters stayed constant at a chosen value, using the Gaussian error propagation. The resulting error (evaluated for an $Al_{0.41}Ga_{0.59}N$ *pin* diode) of

the determined polarization field in dependence of each of its contribution is shown in Fig. 2. With the errors given in Fig. 2, the relative error of the polarization field is 14%. The accuracy of the measurements of the capacitances ($\tilde{C}$, C), the slope of the capacitances ($\partial/\partial V\tilde{C}^{-2}$, $\partial/\partial VC^{-2}$) and the AlGaN layer thickness (d_{DHS}) have a tremendous impact on the accuracy of the polarization field whereas the other parameters have a negligible impact even up to 50% relative error. The accuracy of the AlGaN layer thickness is the dominating error for values exceeding 20% and should be below 10%. Therefore TEM measurements of the AlGaN layer thickness were performed with a high accuracy. Also the measurement error of the reference samples capacitance increases the relative error of the polarization field strongly if it exceeds 7%. We developed, tested, and quantified an advanced equivalent circuit model for the capacitance determination to minimize the error of the capacitance determination and thus of the polarization field determination.

It should be noted that CVM are often based on simplistic circuit models, which do not correctly represent the real device behavior. The capacitance values can be calculated by applying an equivalent-circuit model to the fundamental values. Most LCR Meters have two capacitance measurement methods the C_SR_S and the C_PR_P model. The C_SR_S model assumes a resistor connected in series with the capacitor and neglects all parallel resistors. On the other hand, in the C_PR_P model a resistor connected in parallel with the capacitance is assumed and all serial resistances are neglected. However, *pin* diodes exhibit a series resistance given by the sheet and contact resistances as well as a parallel resistance caused by thermal charge carrier generation in the depletion region (especially in reverse bias), drift and diffusion (in forward bias) and leakage currents via impurity transport or leakage paths along defects.

A major difficulty is that the capacitances and resistances occurring in the *pin* diodes must be known in order to decide which model should be chosen. Assuming a parallel resistance R_p as well as a series resistance R_S in the equivalent circuit to the capacitance of the diode C, the impedance Z can be written as:

$$Z = R_S + \left(\frac{1}{R_P} + 2\pi i f C\right)^{-1}, \tag{4}$$

where i is the imaginary unit and f the frequency. The imaginary part of Eq. (4) is given by:

$$\Im(Z) = -\frac{2\pi f C}{R_P^{-2} + 4\pi^2 f^2 C^2} \tag{5}$$

and can be rewritten to:

$$C = \frac{\frac{\partial}{\partial f}\frac{-f}{2\pi\Im(Z)}}{\frac{\partial}{\partial f}f^2}. \tag{6}$$

Based on the first derivative of the imaginary part of the complex impedance function, Eq. (6) was derived which conveniently eliminates all the resistance terms inclusive those that are voltage dependent as in the case of the *pin* diode resistance.

In order to estimate the error of the capacitance determination, networks of single passive components (resistors and capacitors) were measured and compared to the measurement values of the single capacitors. The circuit has been chosen to be similar to the equivalent circuit of the *pin* diode, with capacitances in the pF range, series resistances in the Ω range and parallel resistances in the MΩ range. The capacitances were evaluated by Eq. (6) and compared to the built-in models of a Keysight E4980A Precision LCR-Meter. In Fig. 3 the deviation from the correct capacitance as a function of the frequency for a *pin* diode-like circuit is shown. The determined capacitance by Eq. (6) shows the smallest deviation from the correct capacitance with a mean error of 1% (see Fig. 3). The C_SR_S and the C_PR_P model show a higher mean deviation of about 2.25%. In order to make statistical statements about the precision of the three models, 70 different combinations of circuits with different capacitances and different resistors were measured. As in Fig. 3, the determination of the capacitance by Eq. (6) is most accurate in almost all cases (especially in all cases where the electrical circuit is similar to the equivalent circuit of a *pin* diode) with an error of 1%–3%.

Therefore, in this paper Eq. (6) was used to determine the capacitance and a relative error of 3% is assumed. Please note that a constant capacitance has been observed for all *pin*-diodes in the possible frequency measurement range (1.4 kHz–2 MHz).

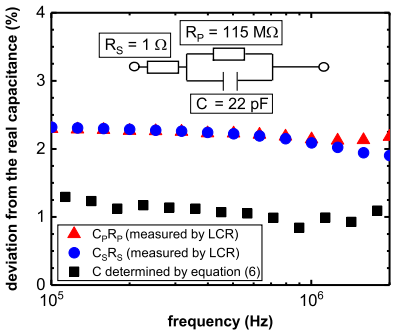

Fig. 3. (Color online) Percentage deviation of the measured values from the correct capacitance value in the frequency range $f = 100$ kHz–2 MHz.

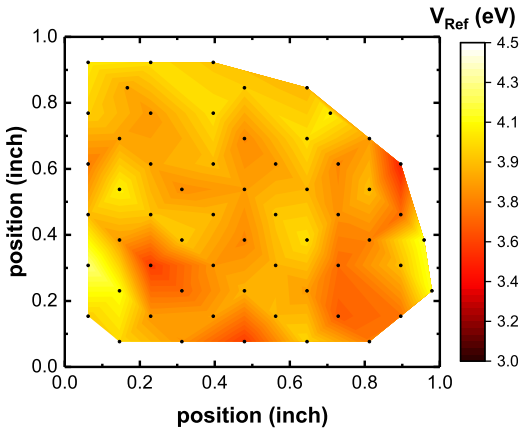

Fig. 4. (Color online) Reference potential as a function of the position on a quarter wafer.

4. Results and discussion

To determine the internal polarization fields with Eq. (1), it is necessary to determine the reference potential V_{ref}. The reference potential V_{ref} was extracted from the CVM of the

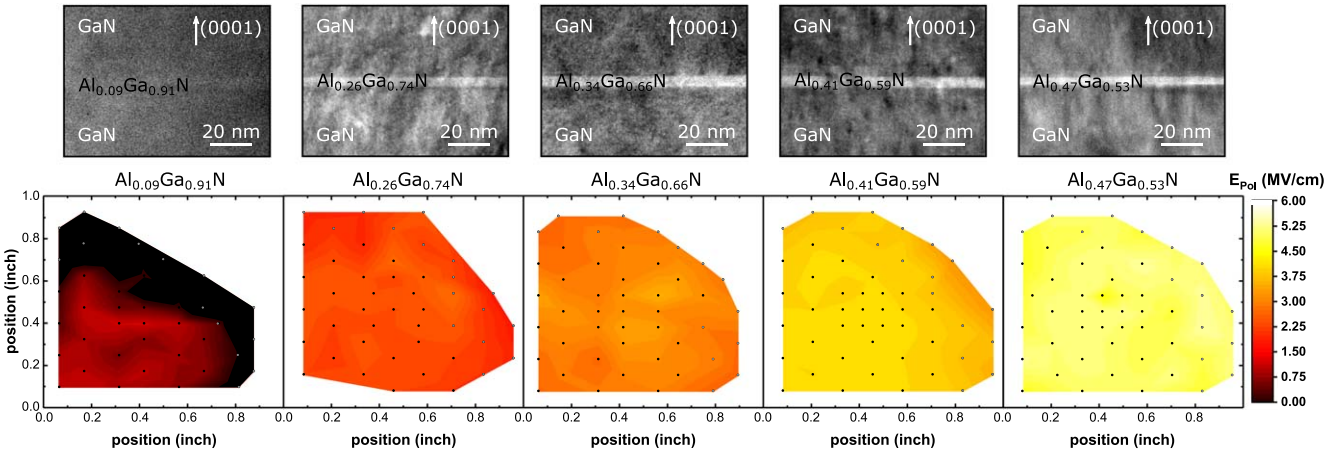

Fig. 5. (Color online) TEM images of the $Al_xGa_{1-x}N$ layer in GaN matrix and internal polarization field of the *pin* diodes as a function of the position on a quarter wafer with different Al-content x. The dots are the location of the measured *pin* diode.

reference sample, i.e. the pin-diode without heterojunction using Eq. (2). The reference potential was evaluated at an AC-frequency of 450 kHz, a DC voltage of 0 V, a temperature of 298 K and an unintentionally n-type doping of $4 \times 10^{16}\,\mathrm{cm}^{-3}$. To reduce the error of a single measurement, 50 *pin* diodes were measured across the wafer. Figure 4 shows the calculated reference potential as a function of the wafer-position. All reference potentials are determined to be between 3.6 and 4.0 eV. On average, a reference potential of $V_{\mathrm{Ref}} = (3.88 \pm 0.26)$ eV with a standard deviation of ±0.16 eV was determined and used to solve the polarization field Eq. (1).

To increase the accuracy of the determination of the internal polarization fields and to confirm the HRXRD of the calibration samples, the $Al_xGa_{1-x}N$ thickness d_{DHS} was measured by TEM. The upper part of Fig. 5 shows the TEM images of the $Al_xGa_{1-x}N$ layer of all samples in the middle of the quarter wafer. In order to determine the $Al_xGa_{1-x}N$ thickness several line-scans along the [0001] crystal direction were performed, also averaging along the [1-100] over 100 nm. Average thicknesses of 4.5 nm ($Al_{0.09}Ga_{0.91}N$), 5.3 nm ($Al_{0.26}Ga_{0.74}N$), 5.2 nm ($Al_{0.34}Ga_{0.66}N$), 5.2 nm ($Al_{0.41}Ga_{0.59}N$), and 4.6 nm ($Al_{0.47}Ga_{0.53}N$) were determined. The TEM results are close to the intended $Al_xGa_{1-x}N$ thickness d_{DHS} of 5 nm. Nevertheless, the measured d_{DHS}, were used to determine the internal polarization field assuming an error of 5% and 10% for the $Al_{0.09}Ga_{0.91}N$/GaN sample due to the low intensity contrast.

The polarization field of 50 *pin* diodes distributed across the sample was determined using Eq. (1). The lower part of Fig. 5 shows the results of the determined polarization field for each measured *pin* diode of the different samples. The maps show that *pin* diodes at the edges provide slightly lower values for the polarization field than *pin* diodes in the center of the sample. Inhomogeneities during the growth of the samples lead to a deviation of the structure on the wafer edge[23] i.e. layer thickness, composition and doping, influencing the capacitance of these diodes and the evaluated polarization fields. Therefore, these *pin* diodes (marked in grey in Fig. 5) were excluded from further evaluations. The mean value from the remaining *pin* diodes within the evaluation range as well as mean error of all errors calculated by Gaussian error propagation were determined (also shown in Fig. 6):

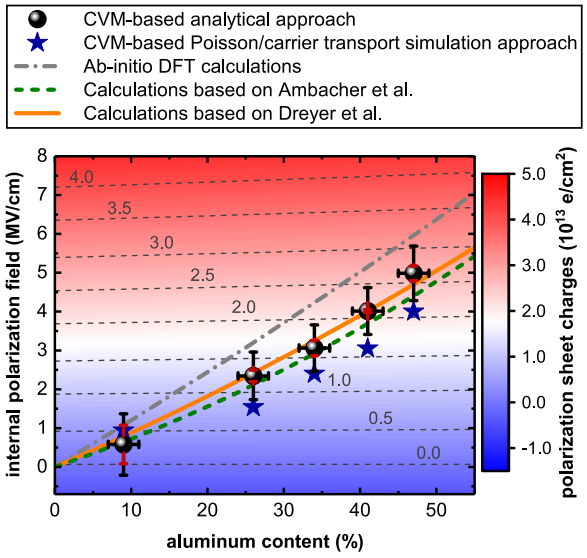

Fig. 6. (Color online) Internal polarization fields determined by capacitance–voltage-measurements (analytical and simulation approach) and theoretically predicted values by Refs. 26, 27, and DFT calculations within this paper. Black dots represent the polarization field averaged over 50 devices with black error bars determined by the error propagation, and the red errors indicating the standard deviation.

$$E_{\mathrm{Pol}}(Al_{0.09}Ga_{0.91}N) = (0.6 \pm 0.7)\,\mathrm{MV\,cm^{-1}}$$
$$E_{\mathrm{Pol}}(Al_{0.26}Ga_{0.74}N) = (2.3 \pm 0.6)\,\mathrm{MV\,cm^{-1}}$$
$$E_{\mathrm{Pol}}(Al_{0.34}Ga_{0.66}N) = (3.1 \pm 0.6)\,\mathrm{MV\,cm^{-1}}$$
$$E_{\mathrm{Pol}}(Al_{0.41}Ga_{0.59}N) = (4.0 \pm 0.7)\,\mathrm{MV\,cm^{-1}}$$
$$E_{\mathrm{Pol}}(Al_{0.47}Ga_{0.53}N) = (5.0 \pm 0.8)\,\mathrm{MV\,cm^{-1}}.$$

Figure 6 does not only show the internal polarization field, but also polarization sheet charges calculated using a simple parallel-plate capacitor model ($E = ne/(\epsilon_0\epsilon_r)$) with a relative dielectric constant for AlN of 9.21[24] and for GaN of 10.04[25] and a linear interpolation for $Al_xGa_{1-x}N$. It is worth noting that due to the dependence of the relative dielectric constant ϵ_r on the aluminum content, the color bar in Fig. 6 is not straight. In addition, Fig. 6 contains also the results of the alternative approach for the polarization field determination that was performed by matching the experimental *CV*-curves with a coupled Poisson-carrier transport simulation (blue stars in Fig. 6). Both approaches are consistent and show the

same trend with overlapping confidence intervals. Although a quantitative error estimation was not possible for the simulation approach, a similar error is expected as also this approach relies on the accuracy of the CVM and the heterostructure thickness measurement. Nevertheless, the CVM-based Poisson-carrier transport simulation approach provides lower internal polarization fields for aluminum contents higher than 9%. Here more investigations are planned to quantify the potential influence of non-abrupt doping profiles and parasitic capacitances on the determined polarization fields by the two methods. We expect that the analytical model is robust against effects adding to the capacitance equally in the reference- and heterostructure *pin* diode as they cancel each other if added in Eqs. (1) and (2).

In order to compare the measured polarization fields to values calculated by density functional theory,[26,27] we determined the lattice constant of the GaN matrix. Due to the different thermal expansion coefficients of GaN and sapphire compressive strain in the GaN matrix may occur at room temperature.[28–30] This strain would lead to a contribution of the piezoelectric polarization field of the GaN matrix. The *a*-lattice constant determining the strain state of the GaN matrix and AlGaN layer was measured by HRXRD. Similarly, based on Ref. 31 several reflections were measured in symmetric and skew symmetric geometry and the lattice constants were calculated accordingly. The *a*- and *c*-lattice constant was determined to be $a_{\mathrm{GaN}}{}^{\mathrm{XRD}} = (3.185\,37 \pm 0.000\,36)$ Å and $c_{\mathrm{GaN}}{}^{\mathrm{XRD}} = (5.187\,78 \pm 0.000\,16)$ Å respectively. The polarization sheet charges are calculated by

$$\sigma_{\mathrm{Pol}} = \Delta P_{\mathrm{SP}} - 2\epsilon_1^{\mathrm{AlGaN}}\left(e_{31}^{\mathrm{AlGaN}} - e_{33}^{\mathrm{AlGaN}}\frac{C_{13}^{\mathrm{AlGaN}}}{C_{33}^{\mathrm{AlGaN}}}\right) + 2\epsilon_1^{\mathrm{GaN}}\left(e_{31}^{\mathrm{GaN}} - e_{33}^{\mathrm{GaN}}\frac{C_{13}^{\mathrm{GaN}}}{C_{33}^{\mathrm{GaN}}}\right), \tag{7}$$

where

$$\epsilon_1 = \frac{a_{\mathrm{GaN}}^{\mathrm{XRD}} - (a_{\mathrm{AlN}}x + a_{\mathrm{GaN}}(1-x))}{a_{\mathrm{AlN}}x + a_{\mathrm{GaN}}(1-x)}, \tag{8}$$

C_{ij} are the elastic constants and a_{AlN} and a_{GaN} are the *a*-lattice constants taken from Ref. 32 respectively. For the spontaneous polarization ΔP_{SP} and piezoelectric polarization constants e_{31} and e_{33} of AlGaN we here compare values published by Refs. 27 and 33.

The orange solid line in Fig. 6 corresponds to the implementation recommended by Ref. 27 i.e. using the layered hexagonal reference structure, the elastic constants from Ref. 34 and the improper piezoelectric constants to determine the polarization sheet charges. Quantities for alloys were obtained using linear interpolation, however with the experimentally measured lattice constants for strain free GaN and AlN and the strained GaN matrix as described above. The polarization sheet charges were converted to internal polarization fields using a simple parallel-plate capacitor model.

The green dashed line in Fig. 6 corresponds to the total internal polarization field predicted by Ref. 26 using the elastic constants and piezoelectric constants from Refs. 33 and 35. The internal polarization fields were calculated by the total electrical polarization ($E_{\mathrm{Pol}} = P/(\epsilon_r - 1)\epsilon_0$) and converted to polarization sheet charges using a simple parallel-plate capacitor model.

However, Refs. 26 and 27 only calculate the binary constants of AlN and GaN. Quantities for alloys were obtained using linear interpolation. A more direct method is to employ the ternary constants from ab initio calculation. We calculated the constants of ternary alloys at compositions of $x = 0$, 0.25, 0.5, 0.75, and 1, after which the second-order polynomial expression was fitted.[36] Then we used the expression to get the spontaneous polarization and piezoelectric polarization constants of $Al_xGa_{1-x}N$ at all compositions. Due to the use of constants of ternary alloys, the grey dashed dotted line in Fig. 6 exhibits a bow. However, compared to Ambacher et al. and Dreyer et al. the bow is rather small and hardly noticeable in the selected scaling.

In conclusion, Fig. 6 shows that the results of the internal field strength and field direction of all samples are in excellent agreement with values predicted by theoretical calculation of ternary alloys giving experimental proof for a nonlinear increasing polarization field with aluminum concentration. The nonlinear dependence on the aluminum concentration *x* can be approximated by a quadratic equation:

$$E_{\mathrm{Pol}}\ (\mathrm{Al}_x\mathrm{Ga}_{1-x}\mathrm{N}) = (6.2x + 9.0x^2)\ \frac{\mathrm{MV}}{\mathrm{cm}}. \tag{9}$$

The degree of agreement between the values predicted by theory and our experimental CV-based approach merits some discussion. For the AlGaN/GaN system, most experimental studies show a significant scatter in the experimental data and an underestimation of the polarization sheet charges compared to the theoretical prediction.[27] Using Eq. (1) to determine the polarization fields has several advantages. Most optical experiments e.g. photoluminescence and electron holography suffer from uncertainties due to screening effects of additionally generated free carriers.[37–40] Measuring the density of the 2DEG by Hall-measurements[2] or capacitance–voltage profiling[41] at the AlGaN/GaN interface can suffer from compensating surface states.[2] In addition, various techniques rely on Schrödinger-Poisson simulations to determine the magnitude of the internal polarization field, and thus suffer from uncertainties in the input parameters.[27,42]

Since our polarization fields were measured in the dark to eliminate any optical excitation and evaluated in the depletion region in low reverse bias, very few carriers in the junction should exist, which was also confirmed by Poisson-carrier transport simulations. However, the CVM-based Poisson-carrier transport simulation approach also considers free carriers. Additionally, the heterostructure is buried deep below the surface and surface states cannot affect the evaluation. Furthermore, by comparing the sample under investigation with a reference sample, the number of input parameters is minimized, and the internal polarization field is mainly given by the difference in the measured capacitances. In addition, by evaluating over 50 *pin* diodes across the wafer, the impact of local defects, growth fluctuations, and process inaccuracies can be minimized. Moreover, in CVM, the non-polarization-induced fields (generated by the *pn* junction, fermilevel pinning, or heterostructure-induced band bending) are described and measured as accurately as possible, while they may not be sufficiently considered by the other methods. In future measurements, the accuracy of the

evaluation method can be further increased using thicker $Al_xGa_{1-x}N$ layers, in order to reduce the influence of thickness fluctuations on the polarization field determination.

5. Conclusions

In this paper we demonstrate the precise determination of polarization fields in $Al_xGa_{1-x}N$ double heterostructures within a GaN matrix based on CVM, by evaluating the changes in the depletion region width of *pin* diodes. The $Al_xGa_{1-x}N$/GaN heterostructures were grown on (0001) sapphire substrates by metalorganic vapor phase epitaxy and fabricated into *pin* diodes by microfabrication techniques. The aluminium content in the $Al_xGa_{1-x}N$ layer was varied between 0.09 and 0.47. A nonlinear increasing polarization field with increasing Al-concentration has been found. The internal polarization fields for $Al_{0.09}Ga_{0.91}N$ (0.6 ± 0.7 MV cm^{-1}), $Al_{0.26}Ga_{0.74}N$ (2.3 ± 0.6 MV cm^{-1}), $Al_{0.34}Ga_{0.66}N$ (3.1 ± 0.6 MV cm^{-1}), $Al_{0.41}Ga_{0.59}N$ (4.0 ± 0.7 MV cm^{-1}) and $Al_{0.47}Ga_{0.53}N$ (5.0 ± 0.8 MV cm^{-1}) in GaN matrix were determined. The results of the internal field strength and field direction of all samples are in excellent agreement with values predicted by theory.

Acknowledgments

This work was supported by the German Federal Ministry of Education and Research (BMBF) within the Advanced UV for Life project and by the Deutsche Forschungsgemeinschaft (DFG) within the Collaborative Research Centre Semiconductor Nanophotonics (SFB 787). Part of this work was also co-funded by the Erasmus+ programme of the European Union. The KAUST authors acknowledge the support of KAUST Baseline BAS/1/1664-01-01, KAUST CRG URF/1/3437-01-01, and GCC REP/1/3189-01-01.

1) H. Hirayama, T. Yatabe, N. Noguchi, and N. Kamata, Electron. Commun. Jpn. **93**, 24 (2010).
2) O. Ambacher et al., J. Appl. Phys. **87**, 334 (2000).
3) O. Ambacher, J. Phys. D: Appl. Phys. **31**, 2653 (1998).
4) P. Ibbetson, P. T. Fini, K. D. Ness, S. P. DenBaars, J. S. Speck, and U. K. Mishra, Appl. Phys. Lett. **77**, 250 (2000).
5) M. Kneissl and J. Rass, *III-Nitride Ultraviolet Emitters: Technology and Applications* (Springer, Berlin, 2016), p. 1.
6) C. Decker, L. Keller, K. Zahouily, and S. Benfarhi, Polymer **46**, 6640 (2005).
7) W. L. Morison, *Phototherapy and Photochemotherapy of Skin Disease* (Raven Press, New York, 1991) 2nd ed., p. 1.
8) M. Kneissl et al., Semicond. Sci. Technol. **26**, 014036 (2010).
9) N. Susilo et al., Appl. Phys. Lett. **112**, 041110 (2018).
10) A. Fujioka, T. Misaki, T. Murayama, Y. Narukawa, and T. Mukai, Appl. Phys. Express **3**, 041001 (2010).
11) C. Pernot et al., Appl. Phys. Express **3**, 061004 (2010).
12) S. Park and S. Chuang, Appl. Phys. Lett. **76**, 1981 (2000).
13) C. Kisielowski et al., Phys. Rev. B **54**, 17745 (1996).
14) A. F. Wright, J. Appl. Phys. **82**, 2833 (1997).
15) A. Bykhovski, B. Gelmont, and M. Shur, J. Appl. Phys. **74**, 6734 (1993).
16) R. Cingolani, A. Botchkarev, H. Tang, H. Morkoc, G. Traetta, G. Coli, M. Lomascolo, A. Di Carlo, F. D. Sala, and P. Lugli, Phys. Rev. B **61**, 2711 (2000).
17) N. Suzuki and N. Iizuka, Jpn. J. Appl. Phys. **38**, L363 (1999).
18) C. Morhain et al., Phys. Rev. B **72**, 241305 (2005).
19) J. S. Im, H. Kollmer, J. Off, A. Sohmer, F. Scholz, and A. Hangleiter, Phys. Rev. B **57**, R9435 (1998).
20) M. Leroux, N. Grandjean, M. Laügt, J. Massies, B. Gil, P. Lefebvre, and P. Bigenwald, Phys. Rev. B **58**, R13371 (1998).
21) N. Susilo et al., J. Phys. D: Appl. Phys. **51**, 485103 (2018).
22) M. Rychetsky et al., J. Appl. Phys. **119**, 095713 (2016).
23) V. Hoffmann, A. Knauer, C. Brunner, S. Einfeldt, M. Weyers, G. Tränkle, K. Haberland, J. T. Zettler, and M. Kneissl, J. Cryst. Growth **315**, 5 (2011).
24) M. Feneberg, M. F. Romero, M. Roppischer, C. Cobet, N. Esser, B. N. K. Thonke, M. Bickermann, and R. Goldhahn, Phys. Rev. B **87**, 235209 (2013).
25) M. Feneberg, S. Osterburg, K. Lange, C. Lidig, B. Garke, and R. Goldhahn, Phys. Rev. B **90**, 075203 (2014).
26) O. Ambacher et al., J. Phys.: Condens. Matter **14**, 3399 (2002).
27) C. Dreyer, A. Janotti, C. Van de Walle, and D. Vanderbilt, Phys. Rev. X **6**, 021038 (2016).
28) T. Detchprohm, K. Hiramatsu, K. Itoh, and I. Akasaki, Jpn. J. Appl. Phys. **31**, L1454 (1992).
29) A. Shikanai, T. Azuhata, T. Sota, S. Chichibu, A. Kuramata, K. Horino, and S. Nakamura, J. Appl. Phys. **81**, 417 (1997).
30) W. Shan, R. J. Hauenstein, A. J. Fischer, J. J. Song, W. G. Perry, M. D. Bremser, R. F. Davis, and B. Goldenberg, Phys. Rev. B **54**, 13460 (1996).
31) M. Frentrup, N. Hatui, T. Wernicke, J. Stellmach, A. Bhattacharya, and M. Kneissl, J. Appl. Phys. **114**, 213409 (2013).
32) H. Angerer et al., Appl. Phys. Lett. **71**, 1504 (1997).
33) F. Bernardini, V. Fiorentini, and D. Vanderbilt, Phys. Rev. B **56**, R10024 (1997).
34) I. Vurgaftman and J. R. Meyer, J. Appl. Phys. **94**, 3675 (2003).
35) A. Zoroddu, F. Bernardini, P. Ruggerone, and V. Fiorentini, Phys. Rev. B **64**, 045208 (2001).
36) K. Liu, F. AlQatari, H. Sun, J. Li, W. Guo, and X. Li, arXiv:1808.07211v2.
37) T. Takeuchi, C. Wetzel, S. Yamaguchi, H. Sakai, H. Amano, I. Akasaki, Y. Kaneko, S. Nakagawa, Y. Yamaoka, and N. Yamada, Appl. Phys. Lett. **73**, 1691 (1998).
38) T. Takeuchi, S. Sota, M. Katsuragawa, M. Komori, H. Takeuchi, H. Amano, and I. Akasaki, Jpn. J. Appl. Phys. **36**, L382 (1997).
39) L. Houben, M. Luysberg, and T. Brammer, Phys. Rev. B **70**, 165313 (2004).
40) C. McAleese, P. M. F. J. Costa, D. M. Graham, H. Xiu, J. S. Barnard, M. J. Kappers, P. Dawson, M. J. Godfrey, and C. J. Humphreys, Phys. Status Solidi B **243**, 1551 (2006).
41) E. T. Yu, G. J. Sullivan, P. M. Asbeck, C. D. Wang, D. Qiao, and S. S. Lau, Appl. Phys. Lett. **71**, 2794 (1997).
42) C. Y. Lai, T. M. Hsu, W. H. Chang, K. U. Tseng, C. M. Lee, C. C. Chuo, and J. I. Chyi, J. Appl. Phys. **91**, 531 (2002).